STRUCTURAL HEALTH MONITORING BY PIEZO-IMPEDANCE TRANSDUCERS. I: MODELING

(AS/2003/022178)

Suresh BHALLA[1] and Chee Kiong SOH [2]

ABSTRACT

The electro-mechanical impedance (EMI) technique, which employs piezoelectric-ceramic (PZT) patches as impedance transducers, has emerged as a powerful NDE technique during the last few years. This series of two papers present a new simplified methodology to diagnose structural damages by means of surface bonded piezo-impedance transducers. The first part introduces a new PZT-structure electro-elastic interaction model based on the concept of 'effective impedance'. The proposed formulations can be conveniently employed to extract the mechanical impedance of any 'unknown' structural system from the admittance signatures of a surface bonded PZT patch. This is an improvement over the existing models, whose complexity prohibits direct application in similar practical scenarios. This also eliminates the requirement of any a-priori information concerning the phenomenological nature of the structure. The proposed model is experimentally verified by means of test on a smart system comprising an aluminum block with a PZT patch instrumented on it. Part II of this paper outlines a new methodology to evaluate structural damages using the extracted impedance spectra. The proposed approach is

[1]**Research Scholar**, Division of Structures and Mechanics, School of Civil and Environmental Engineering, Nanyang Technological University, 50 Nanyang Avenue, Singapore 639798. **Email:** sbhalla@pmail.ntu.edu.sg

[2]**Professor (Corresponding Author)**, Division of Structures and Mechanics, School of Civil and Environmental Engineering, Nanyang Technological University, 50 Nanyang Avenue, Singapore 639798. **Email:** csohck@ntu.edu.sg, **Phone:** (65) 6 790-5306, **Fax:** (65) 6 791-5093.

found to be suitable for diagnosing damages in structures ranging from miniature precision machine and aerospace components to large civil-structures.

KEYWORDS

Damage; electro-mechanical impedance (EMI) technique; structural health monitoring (SHM); non-destructive evaluation (NDE); piezo-electric ceramic (PZT) material.

INTRODUCTION

In spite of substantial improvements in material strength and increased accuracy in analysis and design with the aid of digital computers, gradual deterioration of structures during prolonged usage cannot be completely ruled out. This has been proved by many recent events such as sudden collapse of bridges and in-flight breakdown of aircraft and shuttles, causing immense loss to lives and properties. Hence, the idea of equipping structures with sensors and actuators in an attempt to impart 'smartness' has great potential in cost-effective predictive maintenance of structures, particularly for high performance components not easily accessible for manual inspections. For example, in the aviation sector, many critical aircraft components such as the main landing gear fitting warrant considerable time and effort for dismantling and re-assembling at the time of inspections (Boller 2002). It is estimated that nearly 27% of the aircraft's life cycle cost is spent on inspections and repair (Kessler et al. 2001), which can be significantly brought down by an automated monitoring system. Inspection cum maintenance costs can similarly be reduced for ships, land transport systems, critical machines, dams, bridges, nuclear power plants and skyscraper buildings, whose failure could be extremely devastating for the nation's economy.

Conventionally, automated structural health monitoring (SHM) has been attempted by measuring static displacements (Banan et al. 1994), or static strains (Sanayei and Saletnik 1996) or low frequency vibration data (Pandey and Biswas 1994; Farrar and Jauregui 1998). These techniques typically rely upon conventional sensors such as strain gauges or accelerometers, which can only extract load or strain histories (Giurgiutiu et al. 2000). However, during the last few years, the advent of smart materials, such as piezoelectric materials, optical fibers, shape memory alloys and

magnetostrictive materials, has added a new dimension to SHM, by enabling the development of miniaturized systems with higher resolution, faster response and greater reliability.

During the last seven years, the electro-mechanical impedance (EMI) technique has emerged as a novel non-destructive evaluation (NDE) method, capable of diagnosing practically all types of structures and materials, such as steel bridges (Ayres et al. 1998), reinforced concrete structures (Soh et al. 2000), pipeline structures (Park et al. 2001), pressure vessels (Giurgiutiu et al. 2002), jet engine components (Winston et al. 2001) and thin beams (Tseng and Naidu 2002). In this technique, a piezoelectric-ceramic (PZT) patch is surface bonded to the monitored structure and excited by an alternating voltage sweep signal, typically in kHz range, by an impedance analyzer. The vibrating patch transfers its vibrations to the host structure and simultaneously, the structure influences the electrical circuit comprising the bonded patch and the A.C source. A plot of conductance (real part of admittance) as a function of frequency constitutes a unique vibrational signature of the structure, reflecting structural characteristics such as inherent stiffness, damping and mass distribution. In this manner, the same patch acts as an actuator as well as a sensor. The technique is characterized by a high order of sensitivity to damage (Sun et al. 1995). Typically, in concrete, the piezo-impedance transducers can detect cracks before they actually become visible to the naked eyes (Bhalla and Soh 2003).

This paper presents our new electro-mechanical formulations based on the concept of ‘effective mechanical impedance’, using which the structural impedance can be extracted from the measured admittance signatures for any ‘unknown’ structure. A

new damage quantification methodology will be presented in the second part of this paper.

MECHANICAL IMPEDANCE OF STRUCTURES

A harmonic force, acting upon a structure, can be represented by a rotating phasor on a complex plane (to differentiate it from a vector), as shown in Fig. 1(a). Let F_o be the magnitude of the phasor and let it be rotating anti-clockwise at an angular frequency ω (same as the angular frequency of the harmonic force). At any instant of time 't', the angle between the phasor and the real axis is 'ωt'. The instantaneous force, acting upon the structure, is equal to the projection of the phasor on the real axis i.e. $F_o \cos\omega t$. The projection on the 'y' axis can be deemed as the 'imaginary' component. Hence, the phasor can be represented, using complex notation, as

$$F(t) = F_o \cos\omega t + jF_o \sin\omega t = F_o e^{j\omega t} \tag{1}$$

The resulting velocity response $\dot{u}$, at the point of application of the force, is also harmonic in nature. However, it lags behind the force by a phase angle ϕ, due to the 'mechanical impedance' of the structure. Hence, velocity can also be represented as a phasor, as shown in Fig. 1(a), and expressed as

$$\dot{u} = \dot{u}_o \cos(\omega t - \phi) + j\dot{u}_o \sin(\omega t - \phi) = \dot{u}_o e^{j(\omega t - \phi)} \tag{2}$$

The *mechanical impedance* of the structure, at the point of application of the force, is defined as the ratio of the driving harmonic force to the resulting harmonic velocity at that point. Mathematically, it can be expressed as

$$Z = \frac{F}{\dot{u}} = \frac{F_o e^{j\omega t}}{\dot{u}_o e^{j(\omega t - \phi)}} = \frac{F_o}{\dot{u}_o} e^{j\phi} \tag{3}$$

Based on this definition, the mechanical impedance of a pure mass ‘m’ can be derived as ‘mωj’ (Hixon 1988). Similarly, the mechanical impedance of an ideal spring possessing a spring constant ‘k’ can be derived as ‘–jk/ω’, and that of a damper can be obtained as ‘c’ (the damping constant). For a parallel combination of ‘n’ mechanical systems, the equivalent mechanical impedance is given by (Hixon, 1988)

$$Z_{eq} = \sum_{i=1}^{n} Z_i \tag{4}$$

Similarly, for a series combination,

$$\frac{1}{Z_{eq}} = \sum_{i=1}^{n} \frac{1}{Z_i} \tag{5}$$

Thus, for the parallel combination of a spring-mass-damper system, such as the one shown in Fig. 1(b), we can derive the resultant impedance as

$$Z_{eq} = \sum_{i=1}^{n} Z_i = c + j\left(m\omega - \frac{k}{\omega}\right) \tag{6}$$

The main advantage of the impedance approach is that the differential equations of Newtonian mechanics are reduced to simple algebraic equations and a black-box concept is introduced. Critical forces and velocities only at one or two points of major interest on the structure alone need to be considered, thereby eliminating any complex analysis of the system.

PIEZOELECTRICITY AND ELECTRO-MECHANICAL COUPLING

Piezoelectric Materials

The phenomenon of piezoelectricity occurs in certain classes of non-cento-symmetric crystals, such as quartz, in which electric dipoles (and hence surface charges) are generated due to mechanical deformations. The same crystals also exhibit

the converse effect, that is, they undergo mechanical deformations when subjected to electric fields. The constitutive relations for piezoelectric materials under small field condition are (Sirohi and Chopra 2000)

$$\begin{bmatrix} D \\ S \end{bmatrix} = \begin{bmatrix} \overline{\varepsilon^T} & d^d \\ d^c & \overline{s^E} \end{bmatrix} \begin{bmatrix} E \\ T \end{bmatrix} \tag{7}$$

where **D** (3x1) is the electric displacement vector (C/m^2), **S** (6x1) the strain vector, **E** (3x1) the applied external electric field vector (V/m) and **T** (6x1) the stress vector (N/m^2). $\overline{\varepsilon_{ij}^T} = \varepsilon_{ij}^T(1-\delta j)$ (3x3) is the complex dielectric permittivity at constant stress, d_{im}^d (3x6) and d_{jk}^c (6x3) are the matrices of the piezoelectric strain coefficients and $\overline{s_{km}^E} = s_{km}^E(1-\eta j)$ (6x6) is the matrix of the complex elastic compliance at constant electric field. δ denotes the dielectric loss factor and η the mechanical loss factor. The superscripts ‘T’ and ‘E’ indicate that the quantity has been measured at constant stress and constant electric field respectively. The first subscript denotes the direction of the electric field and the second the direction of the associated mechanical strain. Commercially, the piezoelectric materials are available as ceramics, such as Lead Zirconate Titanate (PZT) and polymers, such as Polyvinvylidene Fluoride (PVDF). The PZT materials, commercially available as thin patches (5-50 mm wide, 0.1-0.5 mm thick), are characterized by high stiffness as well as high piezoelectric strain coefficients, which make them ideal candidates for performing sensing as well as actuating operations in smart structures.

Existing PZT-Structure Interaction Models

Two well-known approaches for modeling the behavior of PZT patch driven electro-mechanical smart systems are the **static** approach and the **impedance** approach. In static approach, proposed by Crawley and de Luis (1987), the PZT patch is assumed to be a thin bar (length '*l*', width 'w', and thickness 'h'), under static equilibrium with the structure, which is represented by its static stiffness K_s, as shown in Fig. 2(a). In this configuration, the PZT constitutive relations (Eq. 7) can be reduced to (Ikeda 1990)

$$D_3 = \overline{\varepsilon_{33}^T} E_3 + d_{31} T_1 \tag{8}$$

$$S_1 = \frac{T_1}{\overline{Y^E}} + d_{31} E_3 \tag{9}$$

where $\overline{Y^E}$ is the complex Young's modulus under constant electric field. Further, due to static conditions, the imaginary component of the complex terms can be dropped. Hence, from Eq. (9), the axial force in the PZT patch can be expressed as

$$F_P = whT_1 = wh(S_1 - d_{31}E_3)Y^E \tag{10}$$

Similarly, the axial force in the structure can be determined as

$$F_S = -K_S x = -K_S l S_1 \tag{11}$$

The negative sign signifies that a positive displacement 'x' causes compressive force in the spring. Force equilibrium in the system implies that

$$F_P = F_S \tag{12}$$

Substituting Eqs. (10) and (11) and solving, we can derive an equilibrium strain, S_{eq}, as

$$S_{eq} = \frac{d_{31}E_3}{\left(1 + K_S l / Y^E wh\right)} \tag{13}$$

Hence, from Eq. (11), the magnitude of the force in the PZT (or the structure) can be worked out as $F_{eq} = K_S l S_{eq}$

In order to determine the response of the system under an alternating electric field, the static approach recommends that a dynamic force with amplitude equal to F_{eq} be applied to the host structure, irrespective of the frequency of actuation. Thus, this approach assumes frequency independent actuator force, determined purely from static equilibrium and strain compatibility between the PZT patch and the host structure. It ignores PZT damping and inertia, which significantly affect PZT output characteristics. Because of these reasons, the static approach often leads to significant errors, especially near the resonant frequency of the structure or the patch. (Liang et al., 1994; Fairweather 1998).

In order to alleviate this inaccuracy, impedance approach was proposed by Liang et al. (1994), based on dynamic equilibrium rather than static equilibrium and by rigorously including dynamic PZT properties and structural stiffness. In this approach, the host structure is represented by its mechanical impedance Z, rather than a pure spring, as shown in Fig. 2(b). The PZT patch is assumed to be a thin bar undergoing axial vibrations under a harmonic electric field E_3. However, dynamic equilibrium is rigorously considered by adopting the governing equation as

$$\overline{Y^E}\frac{\partial^2 u}{\partial x^2} = \rho\frac{\partial^2 u}{\partial t^2} \tag{14}$$

where u is axial displacement at any point in the patch and ρ its material density. The force-displacement relationship for the structure (Eq. 11) is replaced by the force-velocity relationship

$$F_{(x=l)} = -Z\dot{u}_{(x=l)} \tag{15}$$

where Z is defined as the 'drive point mechanical impedance' of the structural system. Further, instead of actuator stiffness, the impedance approach considers actuator impedance Z_a, which is defined as

$$Z_a = \frac{F_{(x=l)}}{\dot{u}_{(x=l)}} = \frac{\kappa w h \overline{Y^E}}{(j\omega)\tan(\kappa l)} \tag{16}$$

where is $\kappa = \omega\sqrt{\rho / Y^E}$ the wave number. Making use of dynamic force equilibrium and the PZT constitutive relations, following generic equation was derived by Liang et al. (1994) for the electrical admittance (inverse of electrical impedance) across the PZT terminals

$$\overline{Y} = G + Bj = \omega j \frac{wl}{h}\left[(\overline{\varepsilon_{33}^T} - d_{31}^2 \overline{Y^E}) + \left(\frac{Z_a}{Z + Z_a}\right) d_{31}^2 \overline{Y_{11}^E}\left(\frac{\tan kl}{kl}\right)\right] \tag{17}$$

Zhou et al. (1995) extended the 1D impedance method to model generic 2D PZT element coupled to a 2D host structure. The related physical model is schematically shown in Fig. 3. The structural impedance is represented by direct impedances Z_{xx} and Z_{yy} and the cross impedances Z_{xy} and Z_{yx}, which are related to the planar forces F_1 and F_2 (in directions 1 and 2 respectively) and the corresponding planar velocities $\dot{u}_1$ and $\dot{u}_2$ by

$$\begin{bmatrix} F_1 \\ F_2 \end{bmatrix} = -\begin{bmatrix} Z_{xx} & Z_{xy} \\ Z_{yx} & Z_{yy} \end{bmatrix}\begin{bmatrix} \dot{u}_1 \\ \dot{u}_2 \end{bmatrix} \tag{18}$$

Applying D'Alembert's principle along the two directions and after imposing the boundary conditions, Zhou et al. (1995) derived

$$\overline{Y} = G + Bj = j\omega \frac{wl}{h}\left[\overline{\varepsilon_{33}^T} - \frac{2d_{31}^2 \overline{Y^E}}{(1-\nu)} + \frac{d_{31}^2 \overline{Y^E}}{(1-\nu)}\left\{\frac{\sin \kappa l}{l} \quad \frac{\sin \kappa w}{w}\right\} N^{-1}\begin{Bmatrix} 1 \\ 1 \end{Bmatrix}\right] \tag{19}$$

where $\kappa = \omega\sqrt{\rho(1-\nu^2)/\overline{Y^E}}$ is the 2D wave number, and N is a 2x2 matrix, given by

$$N = \begin{bmatrix} \kappa\cos(\kappa l)\left\{1-\nu\frac{w}{l}\frac{Z_{xy}}{Z_{axx}}+\frac{Z_{xx}}{Z_{axx}}\right\} & \kappa\cos(\kappa w)\left\{\frac{l}{w}\frac{Z_{yx}}{Z_{ayy}}-\nu\frac{Z_{yy}}{Z_{ayy}}\right\} \\ \kappa\cos(\kappa l)\left\{\frac{w}{l}\frac{Z_{xy}}{Z_{axx}}-\nu\frac{Z_{xx}}{Z_{axx}}\right\} & \kappa\cos(\kappa w)\left\{1-\nu\frac{l}{w}\frac{Z_{yx}}{Z_{pyy}}+\frac{Z_{yy}}{Z_{ayy}}\right\} \end{bmatrix} \quad (20)$$

Z_{axx} and Z_{ayy} are the two components of the mechanical impedance of the PZT patch in the two principal directions.

The mechatronic coupling represented by Eq. (17) or Eq. (19) is employed for damage detection in the EMI technique. The mechanical impedance Z is a function of the structural parameters, which are modified by any structural damage. Consequently, the electromechanical admittance, $\bar{Y}$, will also undergo change and this serves as an indicator of the state of health of the structure. The admittance $\bar{Y}$ (unit Siemens, S, or ohm^{-1}) is a complex quantity, consisting of real and imaginary parts, the conductance (G) and the susceptance (B), respectively.

Limitations of Existing Modeling Approaches

The inability of the static approach in accurately modeling system behavior has already been pointed out in the previous subsection. Although Liang et al. (1994) proposed more accurate formulations using impedance approach, they however ignored the two-dimensional effects associated with PZT vibrations. Their formulations are strictly valid for skeletal structures only, in which all the members are assumed to be 1D and are characterized by negligible stiffness normal to the plane of the structure. However, in other structures, where 2D coupling is significant, Liang's model might introduce serious errors. Zhou et al. (1995) extended Liang's approach to planar vibrations, assuming a four-parameter impedance model for the host structure. Although the analytical derivations of Zhou et al. (1995) are accurate in themselves, the

experimental difficulties prohibit their direct application for extraction of the host structure's mechanical impedance. For example, using the EMI technique, we can experimentally obtain only two quantities- G and B (Eq. 19). If we need to acquire complete information about the structure, we need to solve Eq. (19) for 4 complex unknowns- Z_{xx}, Z_{yy}, Z_{xy}, Z_{yx} (or 8 real unknowns). Thus, the system of equations is highly indeterminate (8 unknowns with 2 equations only). As such, the method could not be employed for the experimental determination of the drive point mechanical impedance.

To alleviate the shortcomings inherent in the existing models, a new concept of 'effective impedance' is introduced in the next section, followed a step-by-step derivation of electro-mechanical admittance across the PZT terminals. The new formulations aim to bridge the gap between 1D model of Liang et al. (1994) and the 2D model of Zhou et al. (1995).

DEFINITION OF EFFECTIVE MECHANICAL IMPEDANCE

Conventionally, mechanical impedance refers to a particular point on the structure. The existing models are based on this definition, the point considered being the PZT end point. However, in reality, the mechanical interaction between the patch and the host structure is not restricted at the PZT end points and it extends all over the finite sized PZT patch.

Consider a finite sized square PZT patch, surface bonded to an unknown host structure, as shown in Fig. 4(a), subjected to a spatially uniform electric field undergoing harmonic variations with time. The patch has half-length equal to '*l*'. Its interaction with the structure is represented in the form of boundary traction 'f' per unit

length, varying harmonically with time. This planar force causes planar deformations in the PZT patch, leading to variations in its surface areaIn the derivations that follow, we assume that the force transmission between the PZT patch and the structure occurs along the entire boundary of the patch, and that plane stress conditions exist within the patch. Besides, the patch is assumed square shaped and infinitesimally small as compared to the host structure, so as to possess negligible mass and stiffness. Opposite edges of the patch, therefore encounter equal dynamic stiffness from the structure, irrespective of the location of the patch on the host structure. Hence, the nodal lines invariably coincide with the two axes of symmetry in the PZT patch, as shown in Fig. 4(b). At the same time, we ignore the effect of the PZT vibrations in the thickness direction, assuming the frequency range of interest to be much lower than the dominant modes of thickness vibration.

. The 'effecive mechanical impedance' of the patch is hereby defined as

$$Z_{a,eff} = \frac{\oint_S \vec{f}.\hat{n}\,ds}{\dot{u}_{eff}} = \frac{F}{\dot{u}_{eff}} \tag{21}$$

where $\hat{n}$ is the unit vector normal to the boundary and 'F' represents the overall planar force (or effective force) causing area deformation of the PZT patch. $u_{\text{eff}} = \delta A/p_o$ is defined as 'effective displacement' of the PZT patch, where δA is the change in the surface area of the patch and p_o its perimeter in the undeformed condition. More precisely, p_o is equal to the summation of the lengths of 'active boundaries', i.e. the boundaries undergoing mechanical interaction with the host structure. Differentiation of the effective displacement with respect to time yields the effective velocity, $\dot{u}_{eff}$. It should be noted that in order to ensure overall force equilibrium, $\oint_S \vec{f} ds = 0$. The

effective drive point (EDP) impedance of the host structure can also be defined on similar lines. However, for determining structural impedance, force needs to be applied on the surface of the host structure along the boundary of the proposed location of the PZT patch.

ELECTRO-MECHANICAL ADMITTANCE FORMULATIONS BASED ON EFFECTIVE IMPEDANCE

Consider the square PZT patch, as shown in Fig. 4(a), under in-plane excitation by a spatially uniform and harmonic electric field, with an angular frequency ω. Since the nodal lines coincide with the axes of symmetry, it suffices to consider the interaction of one-quarter of the patch with the corresponding one-quarter of host structure alone. Let the patch be mechanically and piezoelectrically isotropic in the x-y plane. Hence, $\overline{Y_{11}^E} = \overline{Y_{22}^E} = \overline{Y^E}$ and $d_{31} = d_{32}$. Therefore, the PZT constitutive relations (Eq. 7) can be reduced to

$$D_3 = \overline{\varepsilon_{33}^T} E_3 + d_{31}(T_1 + T_2) \tag{22}$$

$$S_1 = \frac{T_1 - \nu T_2}{\overline{Y^E}} + d_{31} E_3 \tag{23}$$

$$S_2 = \frac{T_2 - \nu T_1}{\overline{Y^E}} + d_{31} E_3 \tag{24}$$

where ν is the Poisson's ratio of the PZT patch. By algebraic manipulation, we can obtain

$$T_1 + T_2 = \frac{(S_1 + S_2 - 2d_{31}E_3)\overline{Y^E}}{1 - \nu} \tag{25}$$

If the PZT patch is in short-circuited condition (i.e. zero electric field),

$$(T_1 + T_2)_{short-circuited} = \frac{(S_1 + S_2)\overline{Y^E}}{1-\nu} \tag{26}$$

As derived by Zhou et al. (1995), the displacements of the PZT patch in the two principal directions are given by

$$u_1 = (A_1 \sin \kappa x) e^{j\omega t} \qquad \text{and} \qquad u_2 = (A_2 \sin \kappa y) e^{j\omega t} \tag{27}$$

where the wave number, $\kappa = \omega\sqrt{\rho(1-\nu^2)/\overline{Y^E}}$ and A_1 and A_2 are constants to be determined from boundary conditions. The corresponding velocities are obtained by differentiating these equations with respect to time.

$$\dot{u}_1 = \frac{\partial u_1}{\partial t} = (A_1 j\omega \sin \kappa x) e^{j\omega t} \quad \text{and} \quad \dot{u}_2 = \frac{\partial u_2}{\partial t} = (A_2 j\omega \sin \kappa x) e^{j\omega t} \tag{28}$$

Similarly, the corresponding strains can be obtained by differentiation with respect to the two coordinate axes.

$$S_1 = \frac{\partial u_1}{\partial x} = (A_1 \kappa \cos \kappa x) e^{j\omega t} \quad \text{and} \quad S_2 = \frac{\partial u_2}{\partial y} = (A_2 \kappa \cos \kappa y) e^{j\omega t} \tag{29}$$

From Fig. 4(b), the effective displacement of the PZT patch, considering displacements at the active boundaries of one-quarter of the patch (the boundaries along the nodal axes are 'inactive' boundaries) is given by

$$u_{eff} = \frac{\delta A}{p_o} = \frac{u_{1o} l + u_{2o} l + u_{1o} u_{2o}}{2l} \approx \frac{u_{1o} + u_{2o}}{2} \tag{30}$$

Differentiating with respect to time, we obtain the effective velocity as

$$\dot{u}_{eff} = \frac{\dot{u}_{1o} + \dot{u}_{2o}}{2} = \frac{\dot{u}_{1(x=l)} + \dot{u}_{2(y=l)}}{2} \tag{31}$$

From Eq. (21), we can obtain the effective impedance of the patch as

$$Z_{a,eff} = \frac{(T_{1(x=l)}lh + T_{2(y=l)}lh)_{short-circuited}}{\left(\frac{\dot{u}_{1(x=l)} + \dot{u}_{2(y=l)}}{2}\right)} \tag{32}$$

Substituting Eqs. (26), (28) and (29) and upon solving, we obtain

$$Z_{a,eff} = \frac{2\kappa lh\overline{Y^E}}{j\omega(\tan kl)(1-\nu)} \tag{33}$$

The overall planar force (or the effective force) F is related to the EDP impedance of the host structure by

$$F = \oint_S \vec{f}.\hat{n}ds = -Z_{s,eff}\dot{u}_{eff} \tag{34}$$

As in the 1D case, negative sign signifies that a positive effective displacement causes compressive force on the patch. Since we are considering square patch, Eq. (34) can be simplified as

$$T_{1(x=l)}hl + T_{2(y=l)}hl = -Z_{s,eff}\left(\frac{\dot{u}_{1(x=l)} + \dot{u}_{2(y=l)}}{2}\right) \tag{35}$$

Substituting Eqs. (25), (28) and (29) and with $E_3 = (V_o/h)e^{j\omega t}$, we get

$$A_1 + A_2 = \frac{2d_{31}V_o Z_a}{(\cos kl)kh(Z_{s,eff} + Z_a)} \tag{36}$$

The instantaneous electric current, which is the time rate of change of charge, can be expressed as

$$\overline{I} = \iint_A \dot{D}_3 dxdy = j\omega \iint_A D_3 dxdy \tag{37}$$

Substituting Eqs. (22), (25) and (29), with $E_3 = (V_o/h)e^{j\omega t}$, and integrating from '$-l$' to '$+l$' with respect to both 'x' and 'y', we can derive $\overline{Y}$, which is the ratio of current to voltage, as

$$\overline{Y} = \frac{\bar{I}}{\overline{V}} = G + Bj = 4\omega j \frac{l^2}{h}\left[\overline{\varepsilon_{33}^T} - \frac{2d_{31}^2\overline{Y^E}}{(1-\nu)} + \frac{2d_{31}^2\overline{Y^E}Z_{a,eff}}{(1-\nu)(Z_{s,eff}+Z_{a,eff})}\left(\frac{\tan\kappa l}{\kappa l}\right)\right] \quad (38)$$

where $\overline{V} = V_o e^{j\omega t}$ is the instantaneous voltage across the PZT patch. Eq. (38) is the desired coupling equation for a square PZT patch. It should be noted that a factor of 4 is introduced in the final expression, since '*l*' here represents half-length of the patch. In the previous models (1D- Liang et al., 1994 and 2D- Zhou et al., 1995), only one half and one-quarter of the PZT patch (from the nodal point to the end of the patch) respectively were considered as the generic elements (See Figs. 2 and 3). The related impedance equations in those models (Eqs. 17 and 19) are valid for one-half and one-quarter of the patch only.

The main advantage of the present approach is that a single complex term for $Z_{s,eff}$ accounts for the two dimensional interactions of the PZT patch with the host structure. This makes the equation simple enough to be utilized for extracting the mechanical impedance of the structure from $\overline{Y}$. The related computational procedure is presented in the second part of this paper.

EXPERIMENTAL VERIFICATION

Details of Experimental Set-up

Fig. 5 shows the experimental test set-up to verify the new effective impedance based electro-mechanical formulations. The test structure was an aluminum block, 48x48x10mm in size, conforming to grade Al 6061-T6 (Young's modulus = 68.95 GPa, Density = 2715 kg/m^3, Poisson's ratio =0.33) . The block was instrumented with a PZT patch, 10x10x0.3mm in size, conforming to grade PIC 151 (PI Ceramic 2003). The patch was bonded to the host structure by means of RS 850-940 epoxy adhesive (RS

Components 1999), and was wired to a HP 4192A impedance analyzer (Hewlett Packard 1996) via a 3499B multiplexer module (Agilent Technologies 2003). In this manner, the electro-mechanical admittance signature, consisting of the real part (conductance- G) and the imaginary part (susceptance- B), was acquired in the frequency range 0-200 kHz.

Determination of EDP Impedance by Finite Element Method (FEM)

Before using Eq. (38) to obtain theoretical signatures for comparison with experimental signatures, we need to evaluate the effective mechanical impedance of the PZT patch ($Z_{a,eff}$) as well as that of the structure ($Z_{s,eff}$). Though a closed form expression has been derived for $Z_{a,eff}$ (Eq. 33), it is not possible to derive such expression for $Z_{s,eff}$ for complex structural systems, especially with non-trivial 3D geometries. This holds true for most real-life structures and systems where NDE is of prime importance. Hence, in this study, a method based on 3D dynamic finite element analysis is developed to determine the EDP impedance of the host-structure. The main strength of the FEM lies in its ability to accurately model real-life complex shapes and boundaries. It should be noted that FEM is solely employed for verifying the new impedance formulations. In actual SHM, no finite element analysis is required, as will be illustrated in the second part of this paper.

The excitation of this smart system by a harmonic electric field is a typical case of linear steady state forced vibrations. Investigations by Makkonen et al. (2001) have shown that fairly accurate results can be obtained for dynamic harmonic problems by FEM, even for frequencies in the GHz range. In FEM, the physical domain (here the volume of the aluminum block) is discretized into elementary volumes called elements

as shown in Fig. 6 for the aluminum block. Because of symmetry about the x and y axes, it suffices to perform computations using only one quadrant of the actual structure. Appropriate boundary conditions were imposed on the planes of symmetry, that is, the x and y components of the displacement were set to zero on the yz and the zx planes of symmetry respectively. The finite element meshing was carried out using the preprocessor tool of ANSYS 5.6 (ANSYS, 2000), with 1mm sized linear 3D brick elements (solid 45), possessing three degrees of freedom at each node. Since the stiffness and the damping of the PZT patch are separately lumped in the term $Z_{a,eff}$ (Eq. 33), we need not mesh the PZT element (Liang et al. 1994). In general, for a forced harmonic structural excitation, Galerkin finite element discretization of the 3D domain leads to (Zienkiewicz 1977)

$$[M][\ddot{u}]+[C][\dot{u}]+[K][u]=[F] \tag{39}$$

where [K] is the stiffness matrix, [M] the mass matrix, [C] the damping matrix, [F] the force vector and $[u]$ the displacement vector. The continuous field quantities i.e. the mechanical displacements are approximated in each of the element through linear sums of the interpolation functions or the shape functions (linear in the present case). The simplest way to determine the EDP impedance is to apply an arbitrary harmonic force (at the desired frequency) on the surface of the structure (along the boundary of the PZT patch), perform dynamic harmonic analysis by FEM, and obtain the complex displacement response at those points. The applied mechanical load (here the effective force F) can be expressed as

$$[\overline{F}]=[F_1+F_2 j]e^{j\omega t} \tag{40}$$

The resulting displacements, which are also harmonic functions of time (at same frequency as the loads) can be similarly expressed as

$$[\bar{u}] = [u_1 + u_2 j]e^{j\omega t} \tag{41}$$

Complex notation is used here to account for the phase lag caused by the 'impedance' of the system (Zienkiewicz 1977). Substituting Eqs. (40) and (41) into Eq. (39) and noting that $[\dot{u}] = j\omega[u]$, $[\ddot{u}] = -\omega^2[u]$, we obtain

$$\{[K] + j\omega[C] - \omega^2[M]\}[u_1 + ju_2] = [F_1 + jF_2] \tag{42}$$

which can be written in a form similar to the static analysis as

$$[A^*][\bar{u}] = [\bar{F}] \tag{43}$$

The only difference from the static case being that all the terms are complex. Eq. (43) can be decomposed into two coupled equations involving real numbers only, and can be solved to obtain the displacement components u_1 and u_2. Then, we can obtain the EDP structural impedance from Eq. (21), noting that $\dot{u}_{eff} = j\omega u_{eff}$ .This solution method is called the full solution method. Reduced solution method (Makkonen et al. 2001) is another approach but it is not as accurate as the full solution method. If the boundary of the PZT patch consists of N equal divisions on each adjacent edge (N = 5 in the present case, as shown in Fig. 6) , we can obtain effective displacement as $\bar{u}_{eff} = \delta A / p_o$, which results in

$$\bar{u}_{eff} = \frac{1}{2}(\bar{u}_{eff,x} + \bar{u}_{eff,y}) \tag{44}$$

where

$$\bar{u}_{eff,x} = \frac{0.5(\bar{u}_{1x} + \bar{u}_{(N+1)x}) + (\bar{u}_{2x} + \bar{u}_{3x} + .. + \bar{u}_{Nx})}{N} \tag{45}$$

and a similar expression can be written for $\bar{u}_{eff,y}$. Further, by splitting the real and the imaginary terms we can alternatively write,

$$\bar{u}_{eff} = \frac{1}{2}(u_{eff,r} + u_{eff,i} j) \tag{46}$$

If a uniformly distributed planar force, with an effective magnitude $\overline{F} = F_r + 0\,j$ is applied, the EDP impedance of the host structure can be derived as

$$Z_{s,eff} = -\left[\frac{2F_r u_{eff,i}}{\omega(u_{eff,r}^2 + u_{eff,i}^2)}\right] - \left[\frac{2F_r u_{eff,r}}{\omega(u_{eff,r}^2 + u_{eff,i}^2)}\right] j \tag{47}$$

This procedure enables the determination of the EDP structural impedance using any commercial FEM software, without any adjustment or including the electric degrees of freedom.

Modeling of Structural Damping

In most commercial FEM software, the damping matrix is determined from the stiffness and the mass matrices as

$$[C] = \alpha[M] + \beta[K] \tag{48}$$

where α is the mass damping factor and β is the stiffness-damping factor. This type of damping is called Rayleigh damping. Further simplification can be achieved by defining damping as a function of the stiffness alone as $[C] = (\eta/\omega)[\mathrm{K}]$, where η is the mechanical loss factor of the material. Then, from Eq. (39), this simplification renders the stiffness matrix complex, as defined by $[\overline{K}] = (1 + \eta j)[K]$. Its equivalent Rayleigh damping coefficients are $\alpha = 0$ and $\beta = \eta/\omega$. In the present analysis considered $\alpha = 0$ and $\beta = 3 \times 10^{-9}$, resulting in $\eta \approx 0.002$ on an average for the frequency range considered.

Wavelength Analysis and Convergence Test

In dynamic harmonic problems, in order to obtain accurate results, a sufficient number of nodal points (3 to 5) per half wavelength should be present in the finite element mesh (Makkonen et al. 2001). In order to ensure this requirement, modal analysis was additionally performed. The frequency range of 0-200kHz was found to contain a total of 24 modes, listed in Table 1 for four different element sizes- 2mm, 1.5mm, 1mm and 0.8mm. It can be observed from the table that good convergence of the modal frequencies is achieved at an element size of 1mm (which is the element size used in the present analysis). Thus, fairly accurate results are expected from the present analysis using FEM. In addition, Figs. 7(a), 7(b) and 7(c) respectively show the plots of the displacements u_x, u_y and u_z, corresponding to the 24^{th} mode (the highest excited mode), over the top surface of the block (z = 10mm). Also, in Fig. 7(d), the displacements in the three principal directions are plotted for the edge AB (see Fig. 6) to illustrate that there are sufficient number of nodes per half wavelength so as to ensure adequate accuracy of the analysis.

Comparison Between Theoretical and Experimental Signatures

Using the EDP structural impedance obtained by FEM, the admittance functions were derived by using Eq. (38). The values of ε_{33}^{T} and δ were determined experimentally. Fig. 8 shows a comparison between the experimental and the theoretical signatures. It is observed that reasonably good agreement exists between the experimental and the analytical plots of the real part- the conductance (Fig. 8a). Major peaks are accurately predicted, though the experimental spectrum contains few unpredicted peaks. However, in the plots of the susceptance (Fig. 8b), large discrepancy

is clearly evident, especially the difference in slopes of the curves. This is attributed to the deviation of the PZT behavior from the ideal behavior predicted by Eq. (33). Besides, many parameters of the PZT patch could deviate from the values provided by the manufacturer. Fortunately, we had obtained the admittance signatures of the PZT patch in 'free-free' condition prior to bonding it on the structure. Hence, it was possible to investigate the behavior of free PZT patch and use this information to obtain more accurate plots. The next section describes the investigations in detail.

REFINING THE MODEL OF PZT SENSOR-ACTUATOR PATCH

The properties of the piezoceramics are strongly dependent upon the process route and exhibit statistical fluctuations within a given batch (Giurgiutiu and Zagrai 2000, caused by inhomogeneous chemical composition, mechanical differences in the forming process, chemical modification during sintering and the polarization method (Sensor Technology Ltd. 1995). A variance of the order of 5-20% in properties is not uncommon. In the EMI technique, we solely depend upon the PZT patches to predict the mechanical impedance spectra of the structures. Hence it is very important to accurately model the behavior of the PZT patches when using the formulations derived in the previous sections. For this purpose, it is recommended that the signatures of the PZT patches be recorded in the 'free-free' condition prior to their bonding on to the host structure.

Looking back at Eq. (38), for a free (unbonded) PZT patch, the complex electro-mechanical admittance can be derived (by substituting $Z_{s,eff} = 0$ and and simplifying) as

$$\overline{Y}_{free} = 4\omega j \frac{l^2}{h}\left[\overline{\varepsilon_{33}^{T}} + \frac{2d_{31}^2 \overline{Y^E}}{(1-\nu)}\left(\frac{\tan \kappa l}{\kappa l} - 1\right)\right] \tag{49}$$

Substituting $\overline{Y^E} = Y^E(1+\eta j)$, $\overline{\varepsilon_{33}^T} = \varepsilon_{33}^T(1-\delta j)$, $(\tan\kappa l/\kappa l) = r + tj$ and $\omega = 2\pi f$ ('f' being the frequency of vibrations in Hz), and simplifying, we get $\overline{Y}_{free} = G_f + B_f j$, where

$$G_f = \frac{8\pi l^2}{h}\left[\varepsilon_{33}^T\delta - \frac{2d_{31}^2 Y_{11}^E}{(1-\nu)}\{\eta(r-1)+t\}\right] \quad \text{and} \quad B_f = \frac{8\pi l^2}{h}\left[\varepsilon_{33}^T + \frac{2d_{31}^2 Y_{11}^E}{(1-\nu)}\{(r-1)-\eta t\}\right] \quad (50)$$

Further, under very low frequencies (typically < one-fifth of the first resonance frequency of the PZT patch), $(\tan\kappa l/\kappa l) \to 1$ (i.e. r→1, t→0) (Liang et al. 1994), thereby leading to quasi-static sensor approximation (Giurgiutiu and Zagrai 2002)

$$G_{f,qs} = \frac{8\pi f l^2 \varepsilon_{33}^T \delta}{h} \quad \text{and} \quad B_{f,qs} = \frac{8\pi f l^2 \varepsilon_{33}^T}{h} \quad (51)$$

Rearranging the various terms, we can write

$$G_{f,qs}^* = \frac{G_{f,qs}h}{8\pi l^2 \varepsilon_{33}^T} = \delta f \quad \text{and} \quad B_{f,qs}^* = \frac{B_{f,qs}h}{8\pi l^2} = \varepsilon_{33}^T f \quad (52)$$

Thus, we can determine the electrical constants ε_{33}^T and δ as the slopes of the frequency plots of $B_{f,qs}^*$ (unit S/m) and $G_{f,qs}^*$ (unit S/F) for sufficiently low frequencies (typically < 10 kHz). Figs. 9 (a) and (b) respectively show the typical plots of these functions in the frequency range 0-10kHz for two PZT patches labelled as S2002-5 and S2002-6. Patch S2002-5 was used as piezo-impedance transducer in the experiment described in the previous section. From these plots, ε_{33}^T was worked out to be 1.7919×10^{-8} F/m and 1.7328×10^{-8} F/m respectively for S2002-5 and S2002-6 (against a value of 2.124×10^{-8} F/m provided by the manufacturer). Similarly, δ was worked out to be 0.0238 and 0.0225 respectively, against a value of 0.015 supplied by the manufacturer.

From these PZT parameters, the conductance and susceptance signatures of the PZT patches s2002-5 and s2002-6 were obtained in the 'free-free' condition in the frequency range 1-1000kHz, using Eq. (50). These are shown in Fig. 10 and compared with the experimental free PZT signatures. Although a quick look at the figures suggests reasonably good agreement between the analytical and the experimental signatures, there are some underlying discrepancies, which need closer examination. For example, a close look in frequency range 0-300kHz (Figs. 10a and 10c) shows an unpredicted mode at around 240kHz. In the case of S2002-5 (Fig. 10a), twin peaks are observed in the experimental spectra around each of the prominent resonance frequencies. Besides, the experimental resonance frequency is slightly higher than the theoretical frequency.

The twin peaks are due to the deviation in the shape of the PZT patch from perfect square shape during manufacturing. This leads to somewhat partly independent peaks corresponding to the two slightly unequal edge lengths. The unpredicted modes in the admittance spectra are due to edge roughness induced secondary vibrations and due to the inability of FEM to accurately model solid-air interactions at the boundaries. Somewhat higher experimental natural frequency suggests additional 2D stiffening, which is unaccounted for in the present model. A similar comparison was reported by Giurgiutiu and Zagrai (2000, 2002), but by considering 1D vibrations only.

Presently, our frequency range of interest is 0-200kHz. The unpredicted mode does not come into picture in this frequency range. In order to 'update' the model of the PZT patch, a correction factor is introduced in the term $\tan(\kappa l)/(\kappa l)$. In the case of PZT patch S2002-5, where twin peaks are observed, this term may be replaced by $\frac{1}{2}\left[\tan(C_1\kappa l)/(C_1\kappa l) + \tan(C_2\kappa l)/(C_2\kappa l)\right]$. By trial and error, values of $C_1 = 0.94$ and $C_2 = 0.883$ were found to be the best. Further, using the techniques of curve fitting, it was

found that $K = 2d_{31}^2 Y^E/(1-\nu) = 5.16x10^{-9}$ NV^{-2} and η = 0.03. The value of K based on data supplied by the manufacturer was determined as $8.4x10^{-9}$ NV^{-2}. Using the experimental values and the correction factors C_1 and C_2, the free PZT signatures were again worked out in the frequency range 0-200kHz. Figs. 11(a) and 11(b) compare the updated signatures with the experimental signatures. A very good agreement is observed between the two. Similarly, for the PZT patch S2002-6, a coefficient C =0.885 was determined, such that the term $(\tan\kappa l/\kappa l)$, when replaced by $\tan(C\kappa l)/(C\kappa l)$ yielded a good agreement between the experimental and the analytical plots of free PZT signatures. Further, K was computed to be $4.63x10^{-9}$ NV^{-2} and η again worked out to be 0.03. Figs. 11(c) and 11(d) compare the analytical and the experimental plots. Again, a good agreement is observed between the experimental signatures and the signatures using the updated PZT model.

As mentioned before, PZT patch S2002-5 was the one bonded to the host structure shown in Fig. 5. The theoretical signatures for this test structure (with the PZT patch bonded on the surface) were again worked out using the updated PZT model. Fig. 12 compares the theoretical and the experimental signatures. This time, a much better agreement is found between the two. Fig. 13(a) compares the idealized and the corrected effective impedance for the patch S2002-5. The influence of twin peaks is clearly reflected in the plot of the updated impedance. If we were to solely depend upon the idealized model of PZT to identify the structure, significant errors could have been introduced, as can be observed from Fig. 13(b).

CONCLUSIONS

This paper has presented a new simplified PZT-structure interaction model based on the concept of effective impedance. As opposed to other impedance-based models, it condenses the two-directional physical coupling between the PZT patch and the structure into a single impedance term, which can be determined from the measured admittance signatures. Hence the model bridges the gap between the 1D impedance model of Liang et al. (1994) and the 2D model proposed by Zhou et al. (1995). Further, a detailed step-by step procedure has been outlined to 'update' the model of the PZT patch before it could be used for 'identifying' the structure. The second part of this paper will present a procedure to extract the mechanical impedance of the structure by means of experimental conductance and susceptance signatures. It will also present a methodology to quantify structural damage using the extracted impedance spectra of the structure on the basis of an equivalent system approach. Besides NDE, the proposed model can be used in numerous other applications, such as predicting the system's response, energy conversion efficiency and system power consumption.

APPENDIX I. REFERENCES

Agilent Technologies (2001). *Test and Measurement Catalogue*, USA.

ANSYS reference manual; release 5.6 (2000). ANSYS Inc., Canonsburg, PA, USA.

Ayres, J. W., Lalande, F., Chaudhry, Z., and Rogers, C.A. (1998). "Qualitative Impedance-Based Health Monitoring of Civil Infrastructures", *Smart Materials and Structures*, 7(5), 599-605.

Banan, M. R., Banan, M. R., and Hjelmstad, K. D. (1994). " Parameter Estimation of Structures from Static Response. I. Computational Aspects", *Journal of Structural Engineering*, ASCE, 120(11), 3243- 3258.

Bhalla, S., and Soh, C. K. (2003). "Structural Impedance Based Damage Diagnosis by Piezo-Transducers*", Earthquake Engineering and Structural Dynamics*, 32(12), 1897-1916.

Boller, C. (2002). "Structural Health Management of Aging Aircraft and Other Infrastructure", *Monograph on Structural Health Monitoring,* Institute of Smart Structures and Systems (ISSS), 1-59.

Crawley, E. F., and de Luis, J. (1987). "Use of Piezoelectric Actuators as Elements of Intelligent Structures", *AIAA Journal*, 25(10), 1373-1385.

Fairweather, J. A. (1998). "Designing with Active Materials: An Impedance Approach", *Ph.D. Dissertation*, Rensselaer Polytechnic Institute, Troy, New York.

Farrar, C. R., and Jauregui, D. A. (1998). "Comparative Study of Damage Identification Algorithms Applied to a Bridge: I. Experiment", *Smart Materials and Structures*, 7(5), 704-719.

Giurgiutiu, V., and Zagrai, A. N. (2000). "Characterization of Piezoelectric Wafer Active Sensors", *Journal of Intelligent Material Systems and Structures*, 11(12), 959-976.

Giurgiutiu, V., Redmond, J., Roach, D., and Rackow, K. (2000). "Active Sensors for Health Monitoring of Aging Aerospace Structures", *Proc. SPIE Conference on Smart Structures and Integrated Systems*, New Port Bleach, 3985, 294-305.

Giurgiutiu, V., and Zagrai, A. N. (2002). "Embedded Self-Sensing Piezoelectric Active Sensors for On-Line Structural Identification", *Journal of Vibration and Acoustics*, ASME, 124(1), 116-125.

Giurgiutiu, V., Zagrai, A. N., and Bao, J. J. (2002). "Embedded Active Sensors for In-Situ Structural Health Monitoring of Thin-Wall Structures", *Journal of Pressure Vessel Technology*, ASME, 124(3), 293-302.

Hewlett Packard (1996). *HP LF 4192A Impedance Analyzer, Operation Manual*, Japan.

Hixon, E.L. (1988). "Mechanical Impedance", *Shock Vibration Handbook*, C. M. Harris, editor, 3rd ed., Mc Graw Hill Book Co., New York, 10.1-10.46.

Ikeda, T. (1990). *Fundamentals of Piezoelectricity*, Oxford University Press, Oxford.

Kessler, S. S., Spearing, S. M., Atala, M. J., Cesnik, C. E. S. and Soutis, C. (2002). "Damage Detection in Composite Materials Using Frequency Response Methods", *Composites, Part B: Engineering*, 33, 87-95.

Liang, C., Sun, F. P., and Rogers, C. A. (1994). "Coupled Electro-Mechanical Analysis of Adaptive Material Systems- Determination of the Actuator Power Consumption and System Energy Transfer", *Journal of Intelligent Material Systems and Structures*, 5(1), 12-20.

Makkonen, T., Holappa, A., Ella, J., and Salomaa, M. (2001). "Finite Element Simulations of Thin-Film Composite BAW Resonators", *IEEE Transactions on Ultrasonics, Ferroelectrics and Frequency Control*, 48(5), 1241-1258.

Pandey, A. K., and Biswas, M. (1994), "Damage Detection in Structures Using Changes in Flexibility", *Journal of Sound and Vibration*, 169(1), 3-17.

Park, G., Cudney, H. H., and Inman, D. J. (2001). "Feasibility of Using Impedance-Based Damage Assessment for Pipeline Structures", *Earthquake Engineering and Structural Dynamics*, 30(10), 1463-1474.

PI Ceramic (2003), *Product Catalogue*, Lindenstrabe, Germany, http://www.piceramic.de, (20 January, 2003)

RS Components (1999), *Product Information Catalogue*, Northants, UK, http://www.rs-components.com, (20January, 2003).

Sanayei, M., and Saletnik, M. J. (1996), "Parameter Estimation of Structures from Static Strain Measurements. I: Formulation", *Journal of Structural Engineering*, ASCE, 122(5), 555-562.

Sensor Technology Limited (1995). *Product Catalogue*, Collingwood.

Sirohi, J., and Chopra, I. (2000). "Fundamental Understanding of Piezoelectric Strain Sensors", *Journal of Intelligent Material Systems and Structures*, 11(4), 246-257.

Soh, C. K., Tseng, K. K. -H., Bhalla, S., and Gupta, A. (2000). "Performance of Smart Piezoceramic Patches in Health Monitoring of a RC Bridge", *Smart Materials and Structures*, 9(4), 533-542.

Sun, F. P., Chaudhry, Z., Rogers, C. A., Majmundar, M., and Liang, C. (1995). "Automated Real–Time Structure Health Monitoring via Signature Pattern

Recognition", *Proc., SPIE Conference on Smart Structures and Materials Conference,* San Diego, California, Feb.27-Mar1, 2443, 236-247.

Tseng, K. K. -H and Naidu, A. S. K. (2002). "Non-Parametric Damage Detection and Characterization using Piezoceramic Material", *Smart Materials and Structures,* 11(3), 317-329.

Winston, H. A., Sun, F., and Annigeri, B. S. (2001). "Structural Health Monitoring with Piezoelectric Active Sensors", *Journal of Engineering for Gas Turbines and Power*, ASME, 123(2), 353-358.

Zhou, S., Liang, C., and Rogers, C.A. (1995). "Integration and Design of Piezoceramic Elements in Intelligent Structures", *Journal of Intelligent material Systems and Structures*, 6(6), 733-742.

Zienkiewicz, O. C. (1977). *The Finite Element Method*, McGraw-Hill Book Company, London.

APPENDIX II. NOTATION

Following symbols are used in this paper

A	=	Area;
B	=	Susceptance;
C	=	Correction factor to update model of PZT;
c	=	Damping constant;
[C]	=	Damping matrix;
D	=	Electric displacement;
d	=	Piezoelectric strain coefficient;

E	=	Electric field;
F	=	Force;
f	=	Boundary traction (per unit length).
G	=	Conductance;
h	=	Thickness of PZT patch;
$\bar{I}$	=	Electric current;
j	=	$\sqrt{-1}$;
k	=	Spring constant;
K	=	Equivalent spring constant of structure;
[K]	=	Stiffness matrix;
l	=	Half-length of PZT patch;
[M]	=	Mass matrix;
p	=	Perimeter;
S	=	Mechanical strain;
T	=	Mechanical stress;
u	=	Displacement;
$\bar{V}$	=	Electric voltage;
w	=	Width of PZT patch;
$\bar{Y}$	=	Complex electro-mechanical admittance;
$\overline{Y^E}$	=	Complex Young's modulus of elasticity at constant electric field;
Z	=	Mechanical impedance;
$\overline{\varepsilon^T}$	=	Complex electric permittivity at constant stress;
ϕ	=	Phase lag;
ω	=	Angular velocity;

ν	=	Poisson’s ratio;
κ	=	Wave number;
α	=	Mass damping factor;
β	=	Stiffness damping factor;
η	=	Mechanical loss factor;
δ	=	Electrical loss tangent;
ρ	=	Material density;

Subscripts

a	=	Actuator;
eff	=	Effective;
o	=	Amplitude of a quantity;
eq	=	Equivalent; Equilibrium;
f, free	=	Free;
i	=	Imaginary;
j,k,l,m	=	Positive integer indices;
r	=	Real;
s	=	Under static conditions;
1,2,3 or x,y,z	=	Coordinate axes;
qs	=	Quasi-static;

Superscripts

T	=	Quantity at constant stress;
E	=	Quantity at constant electric field;

LIST OF FIGURES AND TABLES

(AS/2003/022178)

(c) S2002-6: Conductance vs Frequency.

(d) S2002-6: Susceptance vs Frequency.

Fig. 11 Plots of free-PZT admittance signatures using updated PZT model.

(a) S2002-5: Conductance vs Frequency.

(b) S2002-5: Susceptance vs Frequency

(c) S2002-6: Conductance vs Frequency.

(d) S2002-6: Susceptance vs Frequency.

Fig. 12 Comparison between experimental and theoretical signatures of bonded PZT patch based on updated model of PZT.

(a) Conductance plot. (b) Susceptance plot.

Fig. 13 (a) Comparison between PZT effective impedance predicted by idealised and updated models.

(b) Error in extracted structural impedance in the absence of updated PZT model.

Table 1 Details of modes of vibration of test structure.

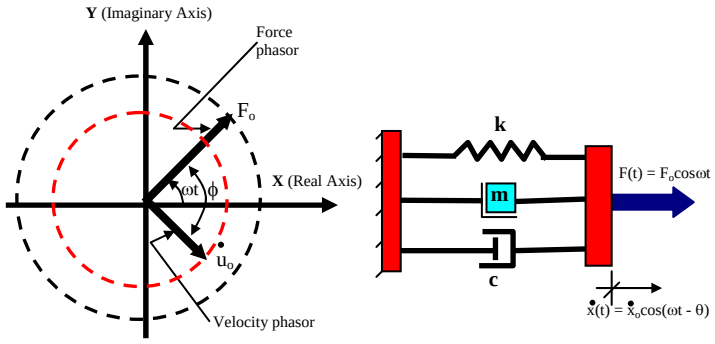

(a) (b)

Fig. 1 (a) Representation of harmonic force and velocity by rotating phasors.

(b) Parallel combination of spring (k), mass (m) and damper (c).

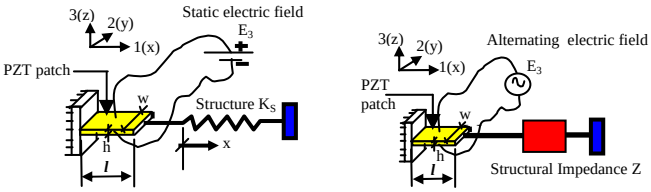

(a) (b)

Fig. 2 Modeling of PZT-structure interaction

(a) Static approach. (b) Impedance approach.

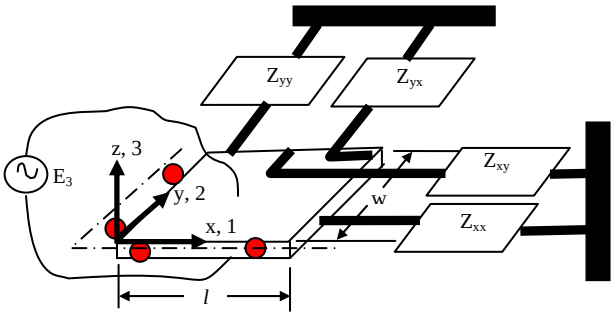

Fig. 3 Modeling of two-way physical coupling by impedance approach.

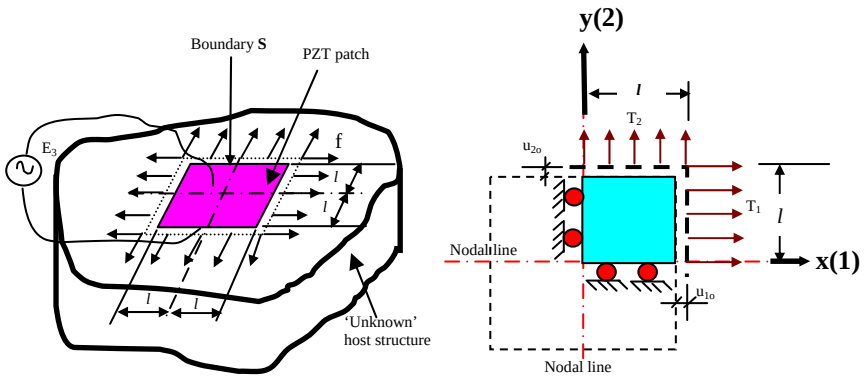

(a) (b)

Fig. 4 (a) A PZT patch bonded to an 'unknown' host structure.

(b) Stresses and displacements on the patch.

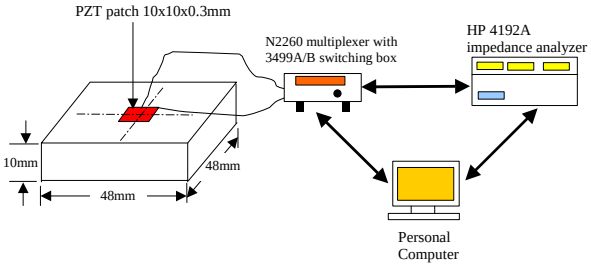

Fig. 5 Experimental set-up to verify new effective impedance based electro-mechanical formulation.

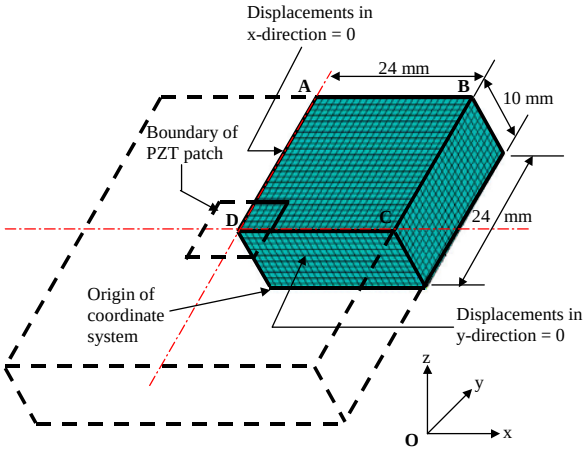

Fig. 6 Finite element model of one-quarter of test structure.

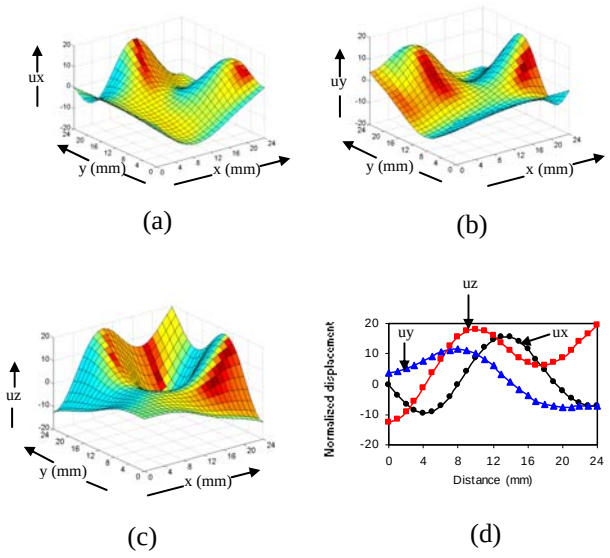

Fig. 7 Examination of mode 24 to check adequacy of mesh size of 1mm

(a) Displacements in x direction on surface z = 10mm.

(b) Displacements in y direction on surface z = 10mm.

(c) Displacements in z direction on surface z = 10mm.

(d) Displacements in principal directions along the line defined by the intersection of surfaces y = 24mm and z = 10mm.

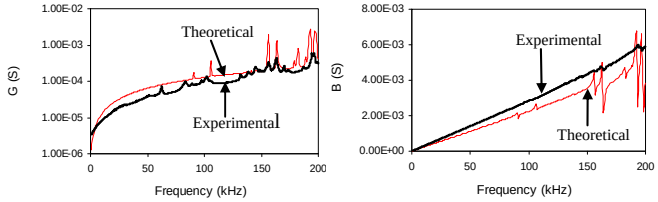

(a) (b)

Fig. 8 Comparison between experimental and theoretical signatures.

(a) Conductance plot. (b) Susceptance plot.

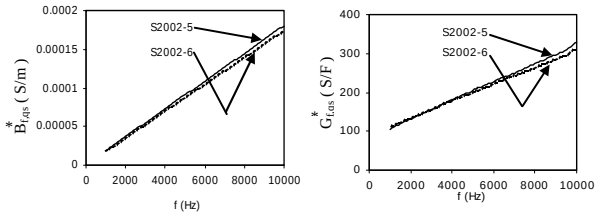

(a) (b)

Fig. 9 Plots of free-PZT quasi-static admittance functions to obtain electric permittivity and dielectric loss factor. (a) $B^*_{f,qs}$. (b) $G^*_{f,qs}$.

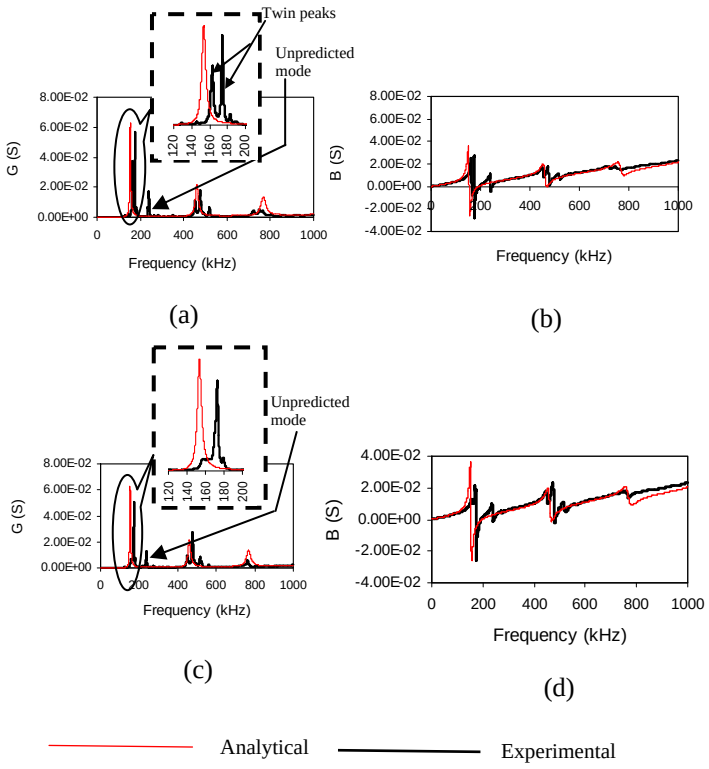

Fig. 10 Experimental and analytical plots of free PZT signatures.

(a) S2002-5: Conductance vs Frequency.

(b) S2002-5: Susceptance vs Frequency

(c) S2002-6: Conductance vs Frequency.

(d) S2002-6: Susceptance vs Frequency.

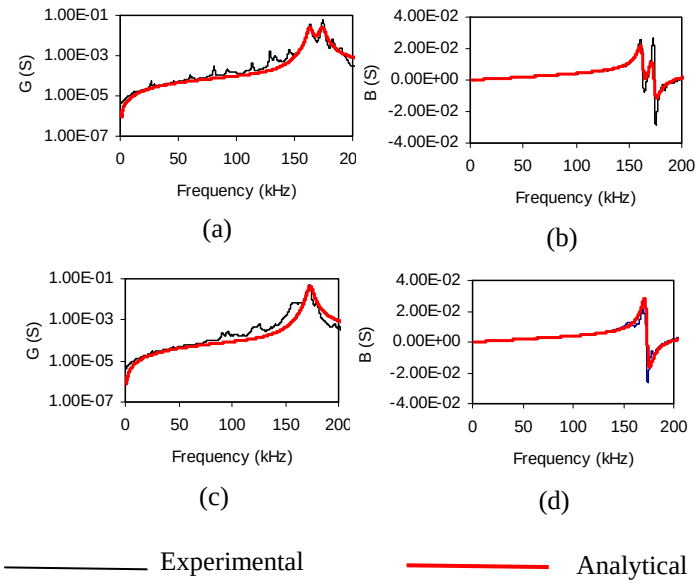

Fig. 11 Plots of free-PZT admittance signatures using updated PZT model.

(a) S2002-5: Conductance vs Frequency.

(b) S2002-5: Susceptance vs Frequency

(c) S2002-6: Conductance vs Frequency.

(d) S2002-6: Susceptance vs Frequency.

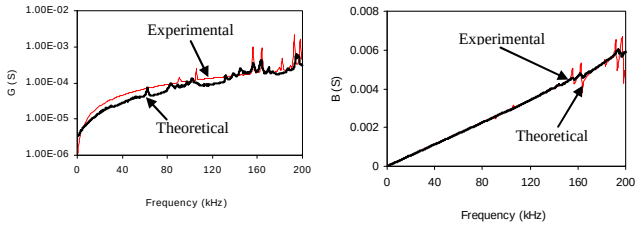

(a) (b)

Fig. 12 Comparison between experimental and theoretical signatures of bonded PZT patch based on updated PZT model

. (a) Conductance plot. (b) Susceptance plot.

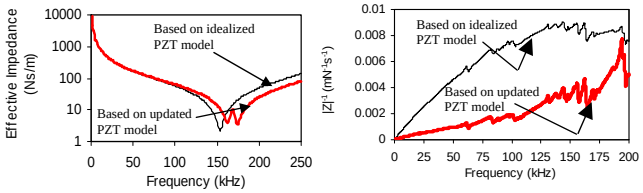

(a) (b)

Fig. 13 (a) Comparison between PZT effective impedance predicted by idealized and updated models.

(b) Error in extracted structural impedance in the absence of updated PZT model.

Table 1 Details of modes of vibration of test structure.

MODE	MODAL FREQUENCY (kHz)				DESCRIPTION OF MODE
	2mm	1.5mm	1mm	0.8mm	
1	81.710	81.480	81.320	81.256	Thickness shear (diagonal)
2	89.354	89.105	88.944	88.884	Face shear
3	90.991	90.765	90.610	90.547	Thickness shear (diagonal)
4	106.667	106.335	106.101	106.016	Face Shear + Flexure
5	125.847	125.125	124.623	124.464	Thickness flexure
6	139.579	138.916	138.521	138.367	Bending about diagonal
7	139.910	139.227	138.845	138.691	Bending about diagonal + Rotation
8	142.425	141.406	140.745	140.525	Thickness Flexure
9	146.653	145.852	145.420	145.249	Flexure
10	148.645	148.017	147.624	147.484	Flexure
11	150.387	149.511	149.000	148.801	Flexure
12	156.807	155.576	154.882	154.623	Flexure
13	157.744	156.706	156.119	155.905	Flexure+Thickness extension
14	165.482	164.333	163.660	163.417	Flexure
15	168.217	166.960	166.207	165.941	Flexure
16	176.823	174.370	172.701	172.186	Thickness flexure
17	181.411	180.035	179.145	178.841	Flexure
18	183.001	181.943	181.222	180.984	Flexure
19	185.590	183.573	182.242	181.808	Flexure
20	191.910	189.760	188.364	187.902	Flexure
21	192.133	190.116	188.776	188.345	Flexure
22	195.335	193.208	191.869	191.424	Flexure
23	196.805	194.432	192.986	192.519	Flexure
24	200.887	199.026	197.845	197.457	Flexure